Optical Fiber Technology 52 (2019) 101985

Contents lists available at ScienceDirect

Optical Fiber Technology

journal homepage: www.elsevier.com/locate/yofte

Imaging through multimode fibers using deep learning: The effects of intensity versus holographic recording of the speckle pattern

Eirini Kakkava[a,*], Babak Rahmani[b], Navid Borhani[a], Uğur Teğin[a,b], Damien Loterie[b], Georgia Konstantinou[b], Christophe Moser[b], Demetri Psaltis[a]

[a] Optics Laboratory, École Polytechnique Fédérale de Lausanne, 1015 Lausanne, Switzerland
[b] Laboratory of Applied Photonic Devices, École Polytechnique Fédérale de Lausanne, 1015 Lausanne, Switzerland

ABSTRACT

Information transmission through multimode fibers (MMFs) has been a topic of great interest for many years. Deep learning algorithms have been applied successfully to MMFs in particular to fiber endoscopy. In this work, we show how Deep Neural Networks (DNNs) can be a versatile technique for classification and recovery of input images that have been significantly distorted while propagating along the MMF forming a speckle pattern. A comparison between holographic and intensity-only recording of the speckle output, which is used as an input to the DNNs, shows that high performance can be achieved without having the full field information (amplitude and phase). Impressive reconstruction fidelity and classification accuracy of the fiber inputs from the intensity-only images of the speckle patterns is reported.

1. Introduction

The idea of imaging using multi-mode fibers (MMFs) has a long history. The earliest report was an experiment done by Spitz and Wertz [1] who phase conjugated the light transmitted through a MMF and obtained a recognizable image back at the input. Several other groups [2–5] reported imaging using MMFs primarily using optical phase conjugation as the mechanism for undoing the distortion that results from modal dispersion as light propagates in a MMF. The development of digital holography [6–10] catalyzed a new wave of developments in imaging using MMFs [11–16]. Digital holography gave unprecedented flexibility in terms of recording and storing large numbers of holograms of the light transmitted through MMFs, allowing us to build databases of input-out pairs of data with which an MMF can be characterized and controlled. Phase conjugation [13,17–19] and the matrix method [14,16,20–26] were deployed to demonstrate various functionalities in MMFs such as focusing [14,22,23,27,28], scanning [16,22], image retrieval [29,30], image projection [31,32], and short pulse delivery [22,23,28] through MMFs. These techniques relied on the linear relationship between the optical fields at the input and the output of the fiber. Impressive demonstrations were carried out, including in-vivo endoscopic imaging [33,34] and several applications were suggested such as laser ablation [22,23], tweezing [31], multi-photon imaging [28,28,35], endoscopy [15,16,23,36,37], 3D printing [19,38]. The major drawback of MMFs when used as an imaging optical element, such as a lens, is the requirement for a calibration step in advance. The database of input-output pairs that is measured and stored digitally is used to interpret the light at the output of the MMF or used to modulate the light at the input of the MMF with a spatial light modulator (SLM). If there is any change in the conditions of the system between the time when the calibration data was collected and when the device is used, then the performance of the system degrades rapidly. In particular bending of the fiber is a major limiting factor for applications that require flexible imaging probes. Several solutions to the bending problem of MMFs have been proposed and demonstrated [12,27,37,39–42]. It is fair to say, however, that at the time of this writing bending remains a major challenge of MMF imaging devices.

The fidelity of the optical transformation performed by the combination of the MMF and SLM has been assessed with phase only modulation, amplitude only modulation and by combinations thereof [22–24,27,43,44]. Although the SLM and MMF system is well described by analytical physical models based on the optical fiber modes, it turns out that in practice, the real fiber index profile deviates from the ideal profile and thus the simple physical model description is not useful when the fiber length is significant (10's of cm). For this reason, in the experimental demonstrations above, the MMF transmission system is treated as a "box" whose transmission matrix must be measured by sending a number of orthogonal pairs of known inputs (and collecting the output) approximately equal to the transmission system's degrees of freedom.

Recently a different approach to approximate the unknown MMF transmission function has been proposed which consists of sending a

* Corresponding author.
E-mail address: eirini.kakkava@epfl.ch (E. Kakkava).

https://doi.org/10.1016/j.yofte.2019.101985
Received 11 May 2019; Received in revised form 16 July 2019; Accepted 19 July 2019
Available online 31 July 2019

large amount of input data (not necessarily orthogonal) compared to the system's degrees of freedom and collecting the output data for the purpose of learning the transmission properties with an artificial neural network. Specifically, Deep Neural Networks (DNNs) have been deployed to model and control MMF imaging devices [45,46]. Generally, DNNs use a database of input-output pairs to train layers of "neurons" to perform the function from which the examples were drawn. We can think of DNNs as an alternative to the matrix or phase conjugation methods for MMF imaging applications. Neural networks model nonlinear systems and therefore they can be used with intensity measurements rather than holographic recordings since they can accommodate the square law nonlinearity. Optical nonlinearities that arise at high intensity levels or nonlinear mappings due to phase modulation by the SLM can also be directly addressed by neural networks. Perhaps most importantly, drifts in the system characteristics (such as bending) can be incorporated in the training set and result in increased robustness in performance. In a recent experiment, imaging through MMFs while bending was demonstrated using DNNs [47]. As another example, temperature and mechanical fluctuations of a 1 km long fiber were partially tolerated in a DNN assisted MMF imaging system [45]. These results indicate potential use of DNNs for real-time endoscopic imaging.

In this paper, we will review the application of DNNs to MMF imaging and highlight some of the recent results from our laboratories. We will start by describing results from recognizing input images to the MMF from the speckle pattern detected at the output and then we concentrate on the classification and reconstruction of the input images. We conclude with a discussion and comparison of DNN techniques with linear methods.

2. Methods

2.1. Optical setup

A standard optical holographic setup (shown in Fig. 1) was used to create the datasets used for training and testing the DNNs on image classification and recovery through MMFs. A diode laser source ($\lambda = 560$ nm) is collimated and split into two paths, by means of a polarizing beam splitter (PBS) which together with a half waveplate (HWP1) adjust the energy ratio of each path. The laser beam in the signal arm is modulated by a phase-only spatial light modulator (SLM, Pluto-NIR2, Holoeye) and imaged onto the proximal fiber facet by means of a 4f-system. A second 4f system is placed at the distal side to image the fiber output on a CCD detector (CCD1, Chameleon 3, 1024 × 1280 pixels, Mono, Point Grey). For monitoring the input on the fiber, we also include a 4f-system to capture the SLM output on a second camera (CCD2). A 2 cm graded-index (GRIN) fiber of 62.5 μm core diameter and NA of 0.275 (by Thorlabs) is used in the experiments presented for the classification performance of the DNNs. In addition, image reconstruction through a 75 cm step-index MMF with a core diameter of 50um (NA = 0.22) is shown in the following sections. In the first case, the fiber supports about 2300 spatial modes and in the second about 1000.

The inputs images are selected from the online available MNIST database of handwritten digits. In each experiment we record 20,000 images of speckle patterns corresponding to each digit projected on the SLM from which 16,000 are used for training the DNNs, 2000 for validation and 2000 for testing the DNN performance. The inputs of the fiber can switch from amplitude (Fig. 2a) to phase (Fig. 2b) and vice-versa by tuning the half waveplate (HWP2) and the polarizer before and after the SLM respectively. In addition, by blocking or not the reference arm we can either detect intensity-only images of the speckle patterns at the fiber output (Fig. 2c) or record the corresponding digital hologram (Fig. 2d) which is formed when the reference beam interferes with the speckle pattern on the CCD1. This configuration allows both amplitude and phase information of the speckle pattern to be obtained at the fiber distal side in order to compare DNNs performance with the intensity-only imaging case.

2.2. Deep neural network architectures

2.2.1. Image classifier

A VGG-type DNN [48], with a convolutional feature detecting frontend and a fully connected backend, was used to classify the recorded distal speckle patterns. The same network architecture (shown in Fig. 3a) with the same hyperparameters was used to process all of the cropped and downsampled speckle images. The datasets comprised 20 k samples which were then randomly separated into 16 k training, 2 k validation, and 2 k testing subsets. The networks were trained using batch sizes of 500 for a maximum of 50 epochs. An Adam optimizer [49] with a 1×10^{-4} learning rate was used to minimize a mean squared error cost function. The network input was either 1 or 2 channel 32 × 32 images. The classification accuracies are reported as the mean and standard deviation of the results of 5 different training instances.

The diameter of the full resolution speckle patterns was 1024 pixels. The recorded speckle images, either intensity only or holographic, were center cropped and down-sampled to 32 × 32 pixels for input into the network.

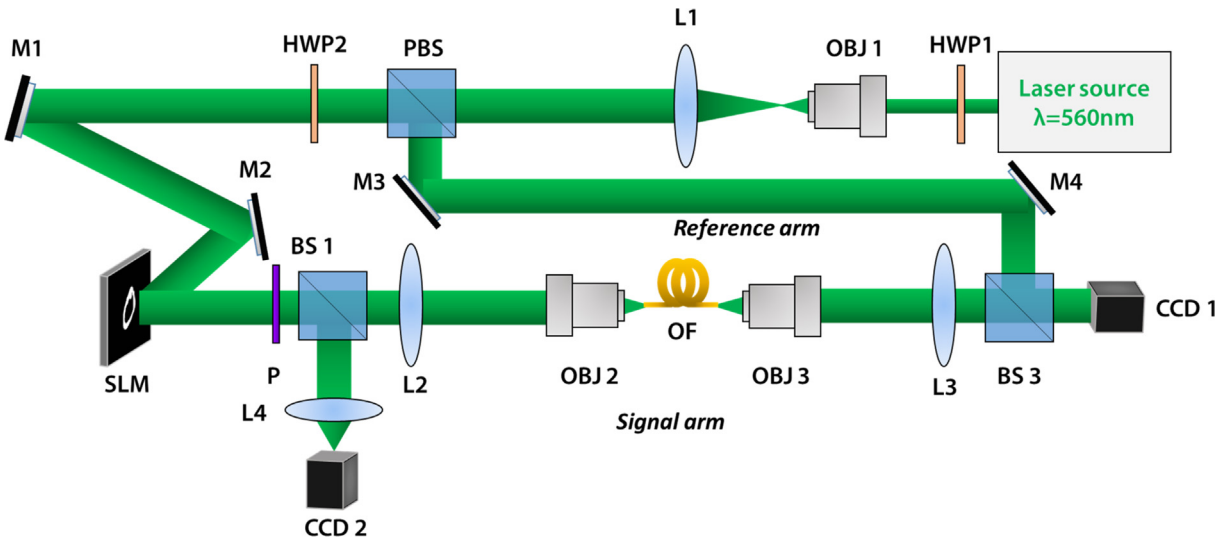

Fig. 1. Optical set for the collection of the datasets consisting of fiber input-output image pairs.

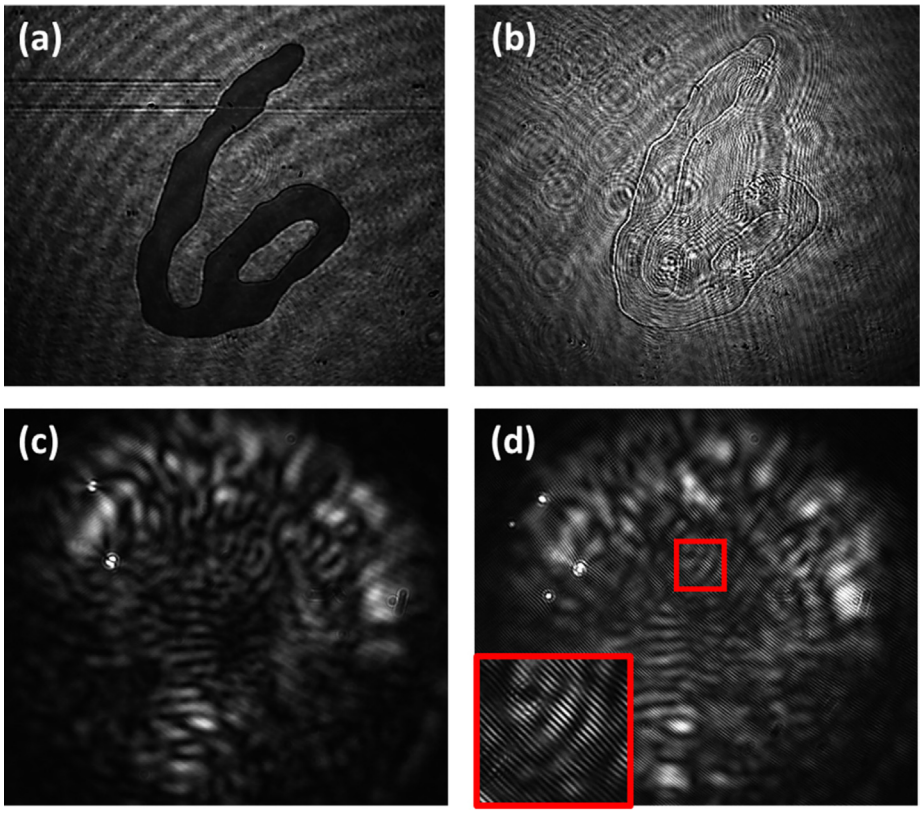

Fig. 2. Image of the SLM output on CCD2 for the digit 6 for a) amplitude and b) phase modulation. Image of the speckle pattern generated at the fiber output for input (b) when the reference beam is c) blocked and d) interfering with the output resulting in a hologram. The inset in image (d) shows a magnified part of the hologram where the interference fringes are clear.

2.2.2. Image reconstruction

The VGG-net is composed of 22 blocks; of which the first and the last are the input and output convolutional units mapping the single channel gray-scale 51 × 51 images to 64 channels and back to one, respectively. The remaining blocks in the middle constitute the hidden unit of the network which does the inverse transformation of either the amplitude-to-amplitude or amplitude-to-phase conversion. The blocks of the hidden unit are composed of two consecutive convolutional units followed by a reshaping unit which up-samples the images by a factor of two and then a max –pooling unit which down-samples the images in each dimension back to the original size. The overall schematic of the network is depicted in Fig. 3b and further explained in our previously published work [46].

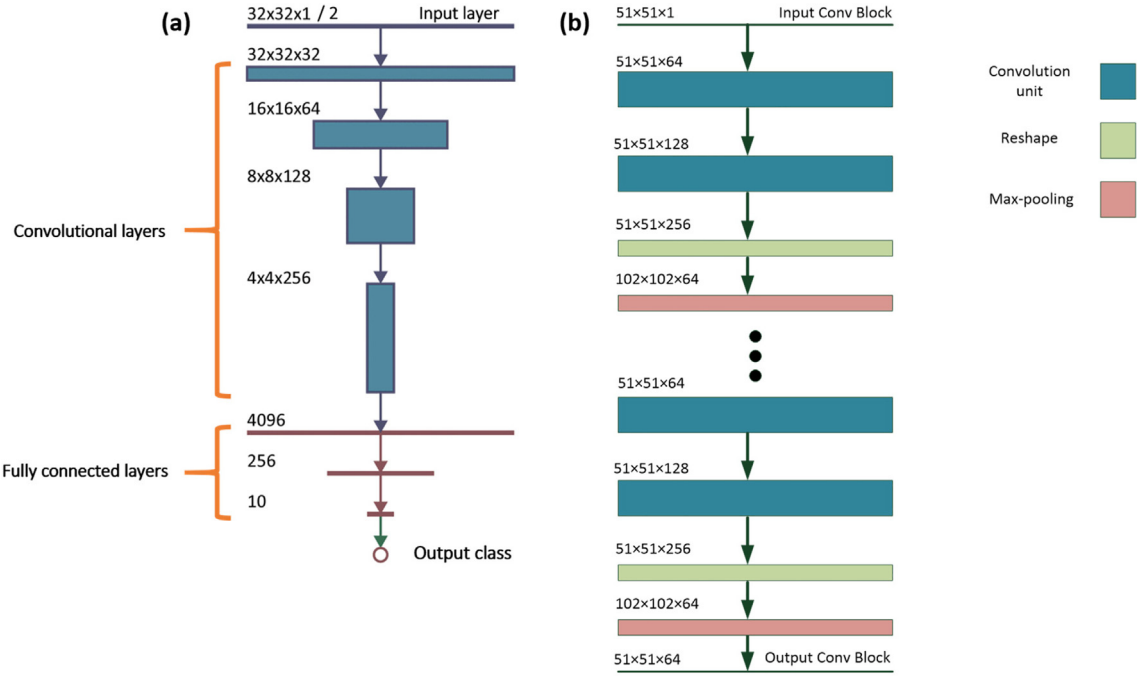

Fig. 3. Scheme of the VGG-type DNN a) classifier architecture and b) reconstruction architecture.

Table 1
Classification accuracies obtained after the DNN is trained with different input images [50]

	Classification accuracy (%)		
VGG network input	# Input channels	Amplitude modulated input	Phase modulated input
Hologram Intensity Fig. 4*(b)*	1	91.8 ± 1.0	93.46 ± 0.6
Amplitude-only Fig. 4*(c)*	1	94.3 ± 0.5	94.2 ± 0.7
Phase-only Fig. 4*(d)*	1	75.2 ± 21.1	75.8 ± 21.8
Real part-only Fig. 4*(e)*	1	91.0 ± 0.8	91.7 ± 0.3
Imaginary part-only Fig. 4*(f)*	1	91.4 ± 0.8	91.7 ± 0.5
Complex Fig. 4*(c&d)*	2	94.0 ± 0.5	94.4 ± 0.3
Complex Fig. 4*(e&f)*	2	92.2 ± 1.1	93.4 ± 0.5
Speckle Intensity	1	92.7 ± 0.5	95.1 ± 0.6

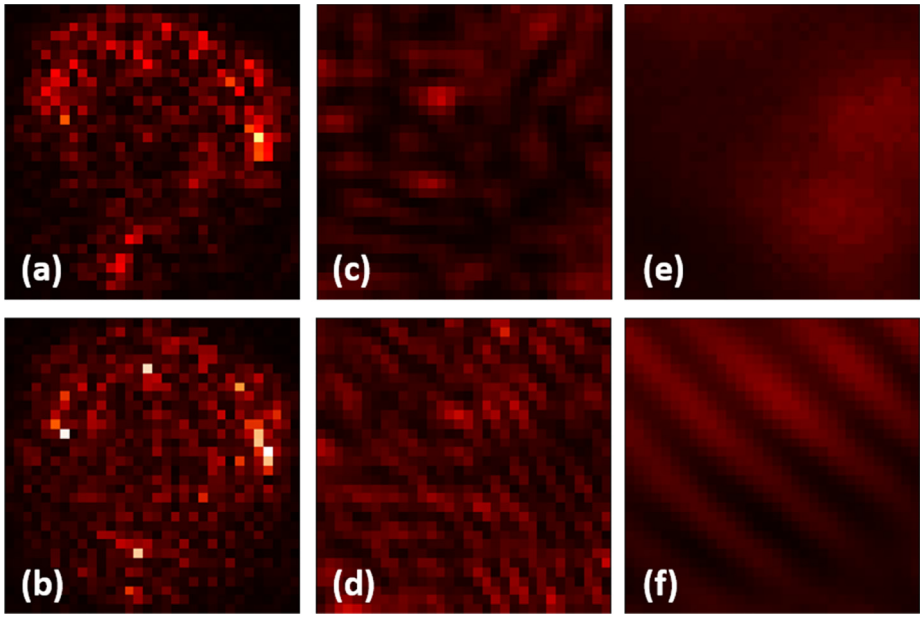

Fig. 4. Cropped images of speckle patterns recorded on the camera CCD1 after downsampling to 32 × 32 pixels. The upper row of images corresponds to intensity-only recording while the lower row to holographic recording of the speckle output. The size of the square cropped area on the initial image changes form 1024 × 1024 pixels a) and b), 256 × 256 pixels c) and d) and 32 × 32 pixels for e) and f).

Table 2
Classification accuracies obtained after the DNN is trained with differently sized cropped portions of the initial speckle image recorded either using intensity-only or holographic measurement.

Crop size [pixels]	Classification accuracy [%]							
	Amplitude modulated - Intensity recording		Phase modulated - Intensity recording		Amplitude modulated - Holographic recording		Phase modulated - Holographic recording	
	Mean	SD	Mean	SD	Mean	SD	Mean	SD
1024 × 1024	93.2	0.7	94.9	0.4	91.8	1	93.5	0.6
512 × 512	91.2	0.8	93	3	89.6	2.2	92.2	1.1
256 × 256	83.2	1.8	91.6	0.4	85.5	1.4	88.3	0.6
128 × 128	76.7	1.4	85.2	0.8	79.8	1.1	83.7	1
64 × 64	66.3	1.9	77.5	1.5	69.2	1.8	73.1	2.3
32 × 32	59.2	2	70.5	2.1	52.9	1.8	63	2

3. Results

3.1. Speckle image classification

The relative classification accuracies provided by intensity or holographic imaging of the speckle patterns, and the combination of different components of the recovered complex field were reported in our previous work [50] and shown in Table 1. The results indicate that intensity only speckle imaging provides similar classification accuracies as for holographic imaging. This greatly simplifies imaging through multimode fibers, since intensity only imaging eliminates the need for the reference arm required for holographic imaging, the post-processing of the holograms to recover the complex fields, and the determination of the transmission matrices.

Since images projected onto the proximal fiber facet are distributed across the propagation modes supported by the fiber, localized image information is spread across the fiber cross-section as it propagates along its length. This spreading of the localized information is further enhanced when the light exits the fiber and interferes to produce the speckle pattern. As a result of this, the intensity of each pixel of the recorded distal speckle pattern is contributed to by large areas of the input images. This contribution is higher for phase modulated inputs where a greater number of the fiber modes are participating in the speckle formation.

Table 3
Classification accuracies obtained after the DNN is trained by cropping different locations on the initial speckle image recorded either using intensity-only or holographic measurement.

Crop location	Classification accuracy [%]							
	Amplitude modulated -Intensity recording		Phase modulated -Intensity recording		Amplitude modulated - Holographic recording		Phase modulated - Holographic recording	
	Mean	SD	Mean	SD	Mean	SD	Mean	SD
1	91.1	0.5	89.6	1.8	86.6	2.3	87.2	1.3
2	90.1	1.8	92.5	1.2	87.1	1	86.7	2.3
3	90.6	1.2	88.7	1.1	85.9	1	87.7	1.1

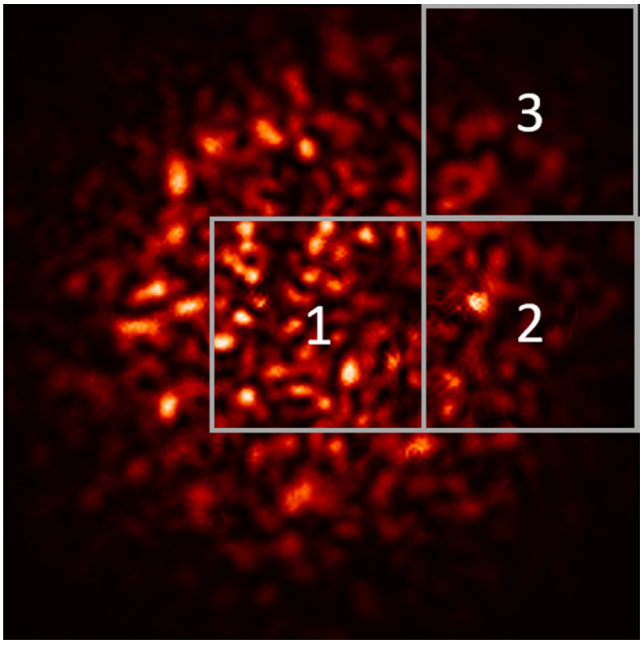

Fig. 5. Image of a speckle pattern recorded at the fiber output. The white square indicate the locations of 340 × 340 pixels crop which are then down-sampled to 32 × 32 pixels for classification by the DNN.

As a result of this spread, it is interesting to assess if there is sufficient information in a cropped area of a speckle image to classify the corresponding input images. In order to study the effects of cropping on the classification accuracy, the full resolution speckle patterns were center cropped to 32, 64, 128, 256, 512, and 1024 pixel sided square areas. These were then down-sampled to 32 × 32 pixel images; examples of these images are shown in Fig. 4. Downsampling of the original speckle pattern results in a blurred version or the initial image. For endoscopic applications this could be also the result of using a partially coherent illumination source. It has been already demonstrated that image reconstruction using an LED source that results in a blurred and almost uniform output of the MMF is possible using DNNs [51].

The results shown in Table 2 indicate that the classification accuracy decreases with decreasing crop sizes for all input modulation and speckle imaging combinations. In particular, for a crop size of 128 × 128 pixels, equivalent to a 1.5% area of the full speckle image, the accuracy decreases by around 12%; whilst for a crop size of 32 × 32 pixels, equivalent to a 0.1% area of the full speckle image, the accuracy decreases by around 30% relative to an uncropped image. Furthermore, Table 3 also shows that phase modulation of the input generally provides higher accuracies than amplitude modulation, probably due to the excitation of more fiber modes. The results also indicate that the combination of phase modulated input and intensity recording of the speckle provides the best results, thus once again highlighting the advantage of using deep learning for multimodal fiber imaging.

In order to study the effects of crop location on the classification accuracy, the full resolution speckle images were cropped to 340 × 340 pixel patches at the three locations shown in Fig. 5. These were then down-sampled to 32 × 32 pixel images for classification by the VGG network. The results, shown in Table 3, indicate that the classification accuracy is essentially independent of crop location on the speckle image, thus highlighting that the input image information is spread over the speckle pattern.

3.2. Speckle image reconstruction

It has been shown that neural networks are able to generalize image transmission inside a MM fiber to other categories of images than the ones used for training the NN. In other words, a neural network trained to reconstruct one class of images can be readily used to retrieve other types of images without the need to further train or fine tune the network. Specifically, it has been shown [46] that a convolutional neural network with the architecture of the VGG networks is able to reconstruct images of digits as well as other drawings when trained only on images of handwritten Latin alphabet. Fig. 6 depicts examples of such reconstructions for both amplitude-output to amplitude-input as well as amplitude-output to phase-input mapping. Ground truth labels are compared against the reconstructed images using the Pearson correlation coefficient (indicated as insets of images). The double nonlinearity of the amplitude to phase inversion is noticeable in the lower fidelity of the amplitude-output to phase-input reconstructed images. In this case, generalization of the network is limited to categories of images with similar features (black background and central features).

However, when trained on a dataset with richer features, the network is expected to generalize better. Fig. 7 plots reconstructed examples of natural images, projected through the MMF as described in previous sections, that were obtained for the ImageNet test dataset when the network is trained on examples from ImageNet train dataset. Here the architecture of the network follows that of the Residual networks which is explained in more details in our previous work [46].

Image reconstruction through MMFs has been studied in the past years using digital holographic approaches such as the transmission matrix (TM) method [14,20,22,22,24]. In order to efficiently reconstruct an image through a MMF the number of supported modes should be at least equal to the number of pixels of the image. The resolution of the endoscope is determined by the wavelength and the NA of the MMF and the signal to noise ratio can be improved by increasing the number of modes. However, contrary to the TM method, image reconstruction using DNNs is not a linear method and the relationship between the fiber modes and the reconstruction fidelity is expected to be different than the one described previously. Nevertheless further investigation is needed in order to define how the DNNs performance changes based on the physical system.

4. Conclusions

This study highlights how recent advances in deep learning have impacted the revival of imaging through multimode fibers. In particular, the deep learning approach has eliminated the need for experimentally determined transmission matrices, and the need for holographic recording of the speckle patterns, thus greatly simplifying its practical implementation. Our studies have shown that image recovery and classification is possible when the DNNs are trained with pairs of input images and their corresponding speckle patterns at the MMF fiber output. In addition, generalization to image sets that the DNN is not trained on is verified to some extent.

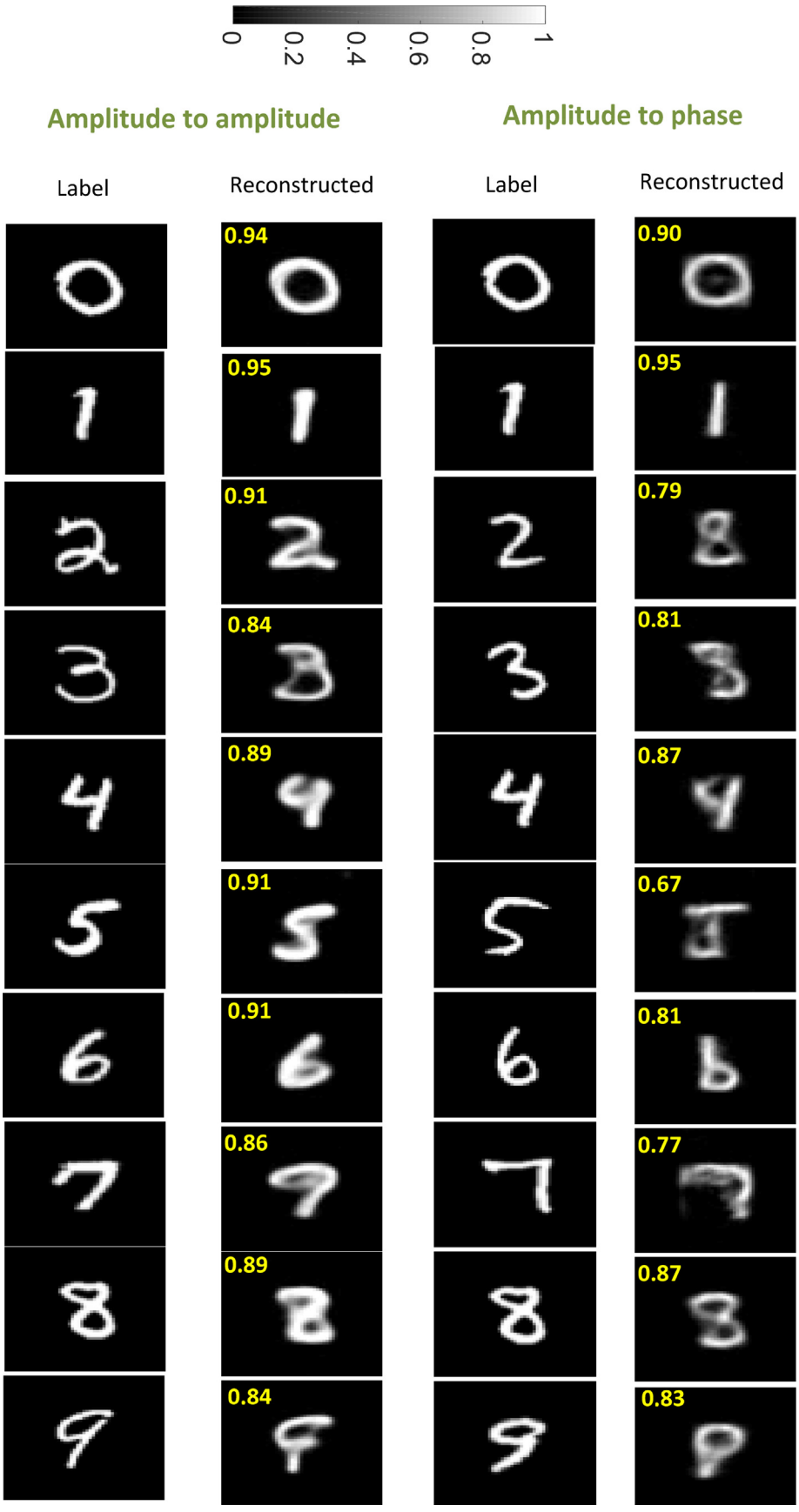

Fig. 6. Image reconstruction of speckle images corresponding to MNIST digit inputs to the MMF using DNNs.

Fig. 7. Reconstruction of image samples from the ImageNet dataset.

Acknowledgments

This project was partially conducted with the support of the Swiss program: CEPF SFA, CERAMIC X.0: High-precision micro-manufacturing of ceramics.

References

[1] E.S.A. Wertz, C. R. Acad. Sci. B 264 (1967) 1015.
[2] A. Gover, C.P. Lee, A. Yariv, J. Opt. Soc. Am. 66 (1976) 306–311.
[3] A.A. Friesem, U. Levy, Y. Silberberg, Proc. IEEE 71 (1983) 208–221.
[4] O.V. Garibyan, I.N. Kompanets, A.V. Parfyonov, N.F. Pilipetsky, V.V. Shkunov, A.N. Sudarkin, A.V. Sukhov, N.V. Tabiryan, A.A. Vasiliev, B. Ya, Zel'dovich, Opt. Commun. 38 (1981) 67–70.
[5] A. Yariv, J. AuYeung, D. Fekete, D.M. Pepper, Appl. Phys. Lett. 32 (1978) 635–637.
[6] J.W. Goodman, Introduction to Fourier Optics, Roberts and Company Publishers, 2005.
[7] Y.-C. Lin, C.-J. Cheng, T.-C. Poon, Appl. Opt. 50 (2011) B25–B30.
[8] I. Yamaguchi, T. Zhang, Opt. Lett. 22 (1997) 1268–1270.
[9] E. Cuche, F. Bevilacqua, C. Depeursinge, Opt. Lett. 24 (1999) 291–293.
[10] C.J. Mann, L. Yu, C.-M. Lo, M.K. Kim, Opt. Express 13 (2005) 8693–8698.
[11] R. Di Leonardo, S. Bianchi, Opt. Express 19 (2011) 247–254.
[12] M. Plöschner, T. Tyc, T. Čižmár, Nat. Photonics 9 (2015) 529.
[13] I.N. Papadopoulos, S. Farahi, C. Moser, D. Psaltis, Opt. Express 20 (2012) 10583–10590.
[14] S. Sivankutty, E.R. Andresen, R. Cossart, G. Bouwmans, S. Monneret, H. Rigneault, Opt. Express 24 (2016) 825.
[15] R.Y. Gu, R.N. Mahalati, J.M. Kahn, Opt. Express 23 (2015) 26905–26918.
[16] Y. Choi, C. Yoon, M. Kim, T.D. Yang, C. Fang-Yen, R.R. Dasari, K.J. Lee, W. Choi, Phys. Rev. Lett. 109 (2012) 203901.
[17] D.B. Conkey, N. Stasio, E.E. Morales-Delgado, M. Romito, C. Moser, D. Psaltis, J. Biomed. Opt. 21 (2016) 045002–045002.
[18] S. Bianchi, R. Di Leonardo, Lab Chip 12 (2012) 635–639.
[19] E.E. Morales-Delgado, L. Urio, D.B. Conkey, N. Stasio, D. Psaltis, C. Moser, Opt. Express 25 (2017) 7031–7045.
[20] S. Popoff, G. Lerosey, M. Fink, A.C. Boccara, S. Gigan, New J. Phys. 13 (2011) 123021.
[21] E.R. Andresen, G. Bouwmans, S. Monneret, H. Rigneault, Opt. Lett. 38 (2013) 609–611.
[22] D.B. Conkey, E. Kakkava, T. Lanvin, D. Loterie, N. Stasio, E. Morales-Delgado, C. Moser, D. Psaltis, Opt. Express 25 (2017) 11491.
[23] E. Kakkava, M. Romito, D.B. Conkey, D. Loterie, K.M. Stankovic, C. Moser, D. Psaltis, Biomed. Opt. Express 10 (2019) 423–433.
[24] D. Loterie, S. Farahi, I. Papadopoulos, A. Goy, D. Psaltis, C. Moser, Opt. Express 23 (2015) 23845–23858.
[25] J. Carpenter, B.J. Eggleton, J. Schröder, Opt. Express 22 (2014) 96.
[26] W. Xiong, P. Ambichl, Y. Bromberg, B. Redding, S. Rotter, H. Cao, Phys. Rev. Lett. 117 (2016) 053901.
[27] A.M. Caravaca-Aguirre, E. Niv, D.B. Conkey, R. Piestun, Opt. Express 21 (2013) 12881.
[28] E.R. Andresen, G. Bouwmans, S. Monneret, H. Rigneault, Opt. Express 21 (2013) 20713–20721.
[29] J.-Y. Son, V.I. Bobrinev, H.-W. Jeon, Y.-H. Cho, Y.-S. Eom, Appl. Opt. 35 (1996) 273–277.
[30] Appl. Phys. Lett. 46 (n.d.) 113–114.
[31] T. Čižmár, K. Dholakia, Nat. Commun. 3 (2012) 1027.
[32] D. Loterie, S.A. Goorden, D. Psaltis, C. Moser, Opt. Lett. 40 (2015) 5754.
[33] S. Turtaev, I.T. Leite, T. Altwegg-Boussac, J.M.P. Pakan, N.L. Rochefort, T. Čižmár, Light Sci. Appl. 7 (2018) 92.
[34] S. Ohayon, A. Caravaca-Aguirre, R. Piestun, J.J. DiCarlo, Biomed. Opt. Express 9 (2018) 1492.
[35] E.E. Morales-Delgado, S. Farahi, I.N. Papadopoulos, D. Psaltis, C. Moser, Opt. Express 23 (2015) 9109.
[36] I.N. Papadopoulos, S. Farahi, C. Moser, D. Psaltis, Biomed. Opt. Express 4 (2013) 260–270.
[37] R. Kuschmierz, E. Scharf, N. Koukourakis, J.W. Czarske, Opt. Lett. 43 (2018) 2997.
[38] P. Delrot, D. Loterie, D. Psaltis, C. Moser, Opt. Express 26 (2018) 1766–1778.
[39] D. Loterie, D. Psaltis, C. Moser, Opt. Express 25 (2017) 6263–6273.
[40] S. Farahi, D. Ziegler, I.N. Papadopoulos, D. Psaltis, C. Moser, Opt. Express 21 (2013) 22504–22514.
[41] M. Lan, D. Guan, L. Gao, J. Li, S. Yu, G. Wu, Opt. Express 27 (2019) 12957–12962.
[42] J. Zhao, Y. Sun, Z. Zhu, J.E. Antonio-Lopez, R.A. Correa, S. Pang, A. Schülzgen, ACS Photonics 5 (2018) 3930–3935.
[43] H. Defienne, M. Barbieri, I.A. Walmsley, B.J. Smith, S. Gigan, Sci. Ad. 2 (2016) e1501054.
[44] A. Drémeau, A. Liutkus, D. Martina, O. Katz, C. Schülke, F. Krzakala, S. Gigan, L. Daudet, Opt. Express 23 (2015) 11898–11911.
[45] N. Borhani, E. Kakkava, C. Moser, D. Psaltis, Optica, OPTICA 5 (2018) 960–966.
[46] B. Rahmani, D. Loterie, G. Konstantinou, D. Psaltis, C. Moser, Light Sci. Appl. 7 (2018) 69.
[47] P. Fan, L. Deng, L. Su, ArXiv:1812.02814 [Physics], 2018.
[48] K. Simonyan, A. Zisserman, ArXiv:1409.1556 [Cs], 2014.
[49] D.P. Kingma, J. Ba, ArXiv Preprint ArXiv:1412.6980, 2014.
[50] E. Kakkava, N. Borhani, C. Moser, D. Psaltis, in: K. Goda, K.K. Tsia (Eds.), High-Speed Biomedical Imaging and Spectroscopy IV, SPIE, San Francisco, United States, 2019, pp. 46.
[51] N. Shabairou, E. Cohen, O. Wagner, D. Malka, Z. Zalevsky, Opt. Lett. 43 (2018) 5603.